



# Experimental determination of effective atomic radii of constituent elements in CrMnFeCoNi high-entropy alloy

Teramoto, Takeshi  
Narasaki, Momoko  
Tanaka, Katsushi

---

## (Citation)

Philosophical Magazine Letters, 102(3):100-110

## (Issue Date)

2022-03-04

## (Resource Type)

journal article

## (Version)

Accepted Manuscript

## (Rights)

This is an Accepted Manuscript of an article published by Taylor & Francis in [Philosophical Magazine Letters on 2022] available online:  
<http://www.tandfonline.com/10.1080/09500839.2021.2024290>

## (URL)

<https://hdl.handle.net/20.500.14094/90009006>



# **Experimental Determination of Effective Atomic Radii of Constituent Elements in CrMnFeCoNi High-Entropy Alloy**

Takeshi Teramoto<sup>a\*</sup>, Momoko Narasaki<sup>a</sup> and Katsushi Tanaka<sup>a</sup>

*<sup>a</sup>Department of Mechanical Engineering, Kobe University, 1-1 Rokkodai-cho, Nada-ku  
Kobe, Hyogo 657-8501, Japan*

E-mail address: [teramoto@mech.kobe-u.ac.jp](mailto:teramoto@mech.kobe-u.ac.jp)

# Experimental Determination of Effective Atomic Radii of Constituent Elements in CrMnFeCoNi High-Entropy Alloy

## Abstract

To elucidate the complex mechanism of solid-solution strengthening in high entropy alloys (HEAs), it is necessary to determine the effective atomic radii of the constituent elements that are the sources of lattice strain. In the present study, the effective atomic radii of the constituent elements in CrMnFeCoNi HEA which is the basis of the atomic displacement are evaluated from the lattice parameters experimentally determined via  $\theta$ - $2\theta$  X-ray diffraction measurements. The order of the evaluated atomic radii in the present study is different from that of the atomic radii determined via ab-initio calculations in previous studies. The results of the ab-initio calculations indicate a correlation between the yield stress of and the average atomic displacement in the HEA. However, no definite correlation is confirmed by the experimental results in the present study.

Keywords: CrMnFeCoNi; High-entropy alloy; Effective atomic radius; Lattice parameter; Atomic displacement;

## 1. Introduction

High-entropy alloys (HEAs) are solid-solution alloys comprising five or more principal constituent elements [1, 2]. HEAs are materials which exhibit attractive properties in terms of high temperature strength [3], ductility [4], fatigue resistance [5], biocompatibility [6], and corrosion resistance [7]. CrMnFeCoNi is a typical HEA with the face-centered cubic (FCC) structure, and its different properties have been previously investigated [8-10]. The mechanical properties of CrMnFeCoNi exhibit a unique temperature dependence [8, 11-13] which distinguishes this alloy from other conventional dilute FCC alloys. Local atomic displacements exist throughout the microstructure of HEAs with high concentrations of multiple elements. These atomic displacements in the matrix, which originate from the solute elements, inhibit the movement of dislocations to strengthen the material. This mechanism of strengthening is termed solid-solution strengthening. However, the conventional solution-strengthening mechanism [14-16] for dilute alloys is not applicable to HEAs. This is because in HEAs, it is difficult to distinguish between the solute and solvent atoms, determine the differences in the radii of multiple atoms, and evaluate the lattice distortion and its overlap. The atomic displacement is confined to the neighboring atoms in dilute alloys. However, all the atoms

in HEAs are displaced from the ideal lattice point, and the average displacement is associated with the yield stress of the material. Atomic displacements have been discussed by experimental and theoretical methods in various HEAs [17-28]. Okamoto et al. [17] experimentally measured the average atomic displacement of the constituents in CrMnFeCoNi via synchrotron X-ray diffraction (XRD) measurements. The mean-squared atomic displacements (MSAD) of the constituents were determined via ab-initio calculations, and the results revealed a correlation between the yield stress and MSAD for the CrMnFeCoNi system. The occurrence of atomic displacement is attributed to the differences in the effective atomic radii of the constituent elements. The atomic radius of each constituent element in a solid solution is different from that of the corresponding isolated element owing to the influence of the surrounding heterogeneous elements. However, there are no reports on the experimental determination of the effective atomic radii of the constituent elements. In the present study, the effective atomic radius of each solute element in an HEA, CrMnFeCoNi, was evaluated from the lattice parameters experimentally determined via  $\theta$ -2 $\theta$  XRD measurements.

## 2. Experimental procedure

Specimens with varying concentrations ( $\pm 5$  at. %) of each solute element were prepared to analyze the composition dependence of the lattice parameters of the individual elements. The compositions of the fabricated specimens are summarized in Table 1a. The alloy ingots were prepared via Ar arc melting. The purity of starting materials is Cr (99.9%), Mn (99.9%), Fe (99.9%), Co (99.9%) and Ni (99.9%), respectively. Each ingot was melted four times, and it was turned over after each melt to ensure homogeneity. Subsequently, the ingot was encapsulated in an evacuated quartz capsule and homogenized at 1373 K for 168 h. Thereafter, it was cold rolling with a rolling rate of 50% and then subjected to solution treatment at 900 °C for 1 h. The cycle of cold rolling and solution treatment was repeated thrice to obtain samples with minor compositional variations. Plate samples of 5 mm  $\times$  5 mm  $\times$  1 mm were cut from the solution-treated sample via FANUC  $\alpha$ -1iC wire electric discharge machining. The sample surfaces were subjected to mechanical polishing using #2000 emery paper as well as chemical polishing using 1  $\mu$ m alumina (Baikalox, Baikowski) and 0.25  $\mu$ m colloidal silica (OP-S, Struers). The compositional analysis of the prepared samples was performed via JEOL JSM-7100F field emission-scanning electron microscopy (SEM) in conjunction with energy-dispersive X-ray spectroscopy (EDS) in 15kV. Thus, the compositional variation within the samples was confirmed to be limited to  $\pm 0.5$  at.%. The average compositions of the prepared samples are summarized in Table 1b.

The lattice parameters were determined via Rigaku UltimaIV Protectus  $\theta$ -2 $\theta$  XRD measurements. LaB<sub>6</sub> (660c, National Institute of Standards and Technology) fine powder was placed on the sample surface as a standard sample to correct the measurement data [29]. Thermal expansion often induces variations in the lattice parameter. To eliminate the influence of such variations, the experimental temperature was maintained at  $22.50 \pm 0.01$  °C using the temperature control stage as shown in Figure 1. A non-reflective Si single-crystal plate was attached to the surface of the stage to eliminate the diffraction peak originating from the stage. The applied voltage and current to the X-ray tube were 40 kV and 40 mA, respectively. A split-type pseudo-Voigt function was adopted for the profile fitting of the obtained data to derive each peak position using a data analysis software (PDXL2, Rigaku). The instrumental error in 2 $\theta$  at each diffraction angle of the standard specimen was evaluated by comparison the diffraction angle obtained with the angle tabulated in the literature [30]. The 2 $\theta$  correction function was obtained by fitting the quadratic function for the 2 $\theta$  angle to the resulting instrumental errors. The measured 2 $\theta$  angle of the specimen were corrected by applying the correction function to eliminate the instrumental error. The lattice parameters were determined using five peaks (2 $\theta$  = 70 – 150°) on the wide-angle side. The lattice spacing of the five peaks was calculated by applying Bragg's law. The lattice parameter was calculated by the relationship between the spacing of the  $hkl$  planes  $d_{hkl}$  and the lattice parameter  $a$  in the cubic crystal ( $a = d_{hkl}(h^2+k^2+l^2)^{1/2}$ ). Generally, a kind of fitting function is applied to get the lattice constant determined at 2 $\theta$  = 180° at which the experimental error becomes zero. However, the present derived lattice constants do not tend to converge towards 2 $\theta$  = 180°. So, the simple average of the derived lattice constants is applied to determine the lattice constant of each specimen.

### 3. Results

Figure 2 presents the XRD patterns of all specimens in Table 1. The lattice parameters are determined from the five peaks hatched in gray. Peaks of the standard sample (LaB<sub>6</sub>) and specimens are shown with indices. Figure 3(a) presents the variations in the lattice parameters for each diffraction peak, while Figure 3(b) presents the determined lattice parameters for all the constituents. The columns headed by + and - in Figure 3(b) present the lattice constants of the constituents from Cr<sup>+</sup> to Ni<sup>+</sup> and Cr<sup>-</sup> to Ni<sup>-</sup>, respectively, with the corresponding standard deviations. The maximum standard deviation of the lattice parameter is approximately 0.1 pm. The composition dependence of the lattice parameter is assumed to have a linear relationship based on the Vegard's law. Though the lattice parameter of a multi-element alloy may show a nonlinear change with

composition, the approximation by the Vegard's law is reasonable as long as the applied composition range is narrow and no strong nonlinearity exists in the composition dependence of the lattice parameter. On the assumption of the linear composition dependence, the determined lattice parameters are subjected to multiple regression analysis; thus, the composition dependence of the effective lattice parameters is estimated. The effective lattice parameter ( $a_{\text{eff}}$ ) is expressed using Eq. 1 based on the multiple regression analysis.

$$a_{\text{eff}} = 357.82 C_{\text{Cr}} + 370.51 C_{\text{Mn}} + 357.56 C_{\text{Fe}} + 352.40 C_{\text{Co}} + 361.23 C_{\text{Ni}} \text{ (pm)}$$

(Eq. 1)

Here,  $C_{\text{Cr}}$ ,  $C_{\text{Mn}}$ ,  $C_{\text{Fe}}$ ,  $C_{\text{Co}}$ , and  $C_{\text{Ni}}$  denote the molar concentrations of Cr, Mn, Fe, Co, and Ni, respectively. The coefficient of determination  $R^2$  value is 0.999 that is close to unity, therefore the predicted lattice parameter shows a reasonable agreement with the experimental one. The relationship between the experimentally determined lattice parameters and the predicted lattice parameters from the regression equation is presented in Figure 4, where the perfect correlation is denoted as a line. The effective lattice parameters of the virtual FCC structure consisting of pure elements are derived from Eq 1. For example, the effective lattice parameter of the FCC lattice consisting of pure Cr is 357.82 pm, which is obtained by substituting the composition of Cr to be 100% in Eq. 1. The effective atomic radius ( $r_{\text{eff}}$ ) is estimated from the effective lattice parameter of the constituent elements by applying the rigid sphere model to the FCC structure. Therefore, the relationship between the effective atomic radius and effective lattice parameter is expressed using the following equation [31]:

$$r_{\text{eff}} = \frac{a_{\text{eff}}}{2\sqrt{2}}$$

(Eq. 2)

The effective lattice parameters and effective atomic radii of the constituent elements in CrMnFeCoNi high entropy alloy at 22.50 °C are summarized in Table 2. The predicted data agree with the experimental one, and the standard error of the effective atomic radii is approximately 0.4 pm. These results indicated that the effective atomic radii are estimated with optimal accuracy.

#### 4. Discussion

#### 4.1 Order of the effective atomic radii

The Goldschmidt radii [32], radii obtained via the ab-initio calculations [17] and effective atomic radii estimated in the present study are summarized in Table 3. The atomic radii in each column are sorted in the ascending order. The atomic radii of the constituent elements in CrMnFeCoNi tend to decrease with an increase in the atomic number; however, the order of the experimentally determined atomic radii is inconsistent with that of the atomic numbers. The Goldschmidt radii are almost the same for each constituent element; furthermore, they do not represent the atomic radii of the elements in HEAs. The difference between the maximum and minimum atomic radii determined via the ab-initio calculations is similar to that between the maximum and minimum atomic radii determined in the present experiment. However, the order of the experimentally determined atomic radii is different from that of the atomic radii obtained via the ab-initio calculations. One of the considerable reasons for the discrepancy is the effect of thermal vibrations of the constituent atoms. The linear expansion coefficient and the temperature sensitivity of Mn are higher than those of the other elements [33]. Mn exhibited temperature-sensitive variations in the atomic radius. Consequently, the experimentally determined effective atomic radius of Mn is larger than that of the other elements.

#### 4.2 Relationship between the strength and the lattice strain

To understand the effect of solid-solution strengthening on the strength of HEAs, it is important to discuss the relationship between the lattice strain and the strength. Here, we discuss the relationship between the strength and the lattice strain of HEAs on the assumption that the constituent elements in the ternary, quaternary, and quinary alloys exhibited similar atomic radii. The yield stresses of quaternary and ternary alloys in the CrMnFeCoNi alloy system have been previously investigated [10]. The CrMnFeCoNi alloy system includes CrMnFeCoNi, MnFeCoNi, CrFeCoNi, CrMnCoNi, CrCoNi, MnFeNi, MnCoNi, and FeCoNi with FCC structures [9]. The relationship between the yield stress and the atomic displacement for these FCC alloys is investigated in the present study. The average atomic displacement is calculated from the experimental and the ab-initio calculations results reported by Okamoto et al. [17]. To evaluate the MSAD, it is necessary to obtain the static displacement of each constituent atom from its ideal lattice point, therefore, the MSAD is not able to calculate from the effective atomic radius obtained in this study. Alternatively, the  $\delta$  parameter [34] is commonly used as a parameter to evaluate the magnitude of atomic displacement in HEA. The  $\delta$  parameter denotes the average squared displacement of each atom from the FCC lattice point, and

it can be expressed using the following equation [34]:

$$\delta r = \sqrt{\frac{1}{n} \sum_i (r_i - \bar{r})^2}$$

(Eq. 3)

Here,  $n$ ,  $r_i$ , and  $\bar{r}$  denote the number of elements in the HEA, effective atomic radius of each element, and the average effective atomic radius, respectively. The relationship between the yield stress and the average atomic displacement is presented in Figure 5. The correlation coefficient between the yield stress and the  $\delta r$  from ab-initio calculations [17] is 0.90, indicating a positive correlation as denoted by the filled dots in the gray circle. However, the correlation coefficient between the yield stress and the  $\delta r$  from the experimental results is -0.31, which indicates that there is no correlation. Therefore, at least the  $\delta$  parameter at room temperature does not explain the strength of the HEA alloy system. The difference between the ab-initio calculations [17] and the experimental results can be attributed to the fact that the effective atomic radius of Mn, which has a large linear thermal expansion coefficient, is larger than that of other constituent elements due to the effect of thermal vibration of atoms [33]. It is thought that the correspondence between the experimental values and the first-principle calculation results can be clarified by considering the linear expansion coefficient of CrMnFeCoNi, however, further investigation is needed in this point.

## Conclusion

The effective atomic radii of the constituent elements in an HEA, CrMnFeCoNi, are estimated from the lattice parameters experimentally determined via  $\theta$ -2 $\theta$  XRD. Multiple regression analysis, based on the composition dependence of the lattice parameters, is performed to calculate the effective lattice parameters with optimal accuracy. The effective atomic radii are calculated from the effective lattice parameters with minimal errors ( $\sim 0.4$  pm). The order of the experimentally determined effective atomic radii is different from that of both the Goldschmidt radii and the radii obtained via the ab-initio calculations. The  $\delta$  parameter calculated from the obtained effective atomic radii indicate no definite correlation to the yield stress.

## Declaration of Competing Interest



The authors declare that they have no known competing financial interests or personal relationships that could have appeared to influence the work reported in this paper.

## Acknowledgement

This study is based on work supported by the Grant-in-Aid for Scientific Research (ID: 19H05174) through the Japan Society for the Promotion of Science (JSPS).

## References

- [1] J.W. Yeh, S.K. Chen, S.J. Lin, J.Y. Gan, T.S. Chin, T.T. Shun, C.H. Tsau, and S.Y. Chang, *Nanostructured High-Entropy Alloys with Multiple Principal Elements: Novel Alloy Design Concepts and Outcomes*, *Advanced Engineering Materials* 6 (2004), pp. 299-303.
- [2] J.W. Yeh, Y.L. Chen, S.J. Lin, and S.K. Chen, *High-Entropy Alloys – A New Era of Exploitation*, *Materials Science Forum* 560 (2007), pp. 1-9.
- [3] O.N. Senkov, G.B. Wilks, J.M. Scott, and D.B. Miracle, *Mechanical properties of Nb<sub>25</sub>Mo<sub>25</sub>Ta<sub>25</sub>W<sub>25</sub> and V<sub>20</sub>Nb<sub>20</sub>Mo<sub>20</sub>Ta<sub>20</sub>W<sub>20</sub> refractory high entropy alloys*, *Intermetallics* 19 (2011), pp. 698-706.
- [4] S.S. Nene, P. Agrawal, M. Frank, A. Watts, S. Shukla, C. Morpew, A. Chesetti, J.S. Park, and R.S. Mishra, *Transformative high entropy alloy conquers the strength-ductility paradigm by massive interface strengthening*, *Scripta Materialia* 203 (2021).
- [5] W. Li, S. Chen, and P.K. Liaw, *Discovery and design of fatigue-resistant high-entropy alloys*, *Scripta Materialia* 187 (2020), pp. 68-75.
- [6] W.-Y. Ching, S. San, J. Brechtel, R. Sakidja, M. Zhang, and P.K. Liaw, *Fundamental electronic structure and multiatomic bonding in 13 biocompatible high-entropy alloys*, *npj Computational Materials* 6 (2020).
- [7] Y. Zhang, T.T. Zuo, Z. Tang, M.C. Gao, K.A. Dahmen, P.K. Liaw, and Z.P. Lu, *Microstructures and properties of high-entropy alloys*, *Progress in Materials Science* 61 (2014), pp. 1-93.
- [8] B. Cantor, I.T.H. Chang, P. Knight, and A.J.B. Vincent, *Microstructural development in equiatomic multicomponent alloys*, *Materials Science and Engineering a-Structural Materials Properties Microstructure and Processing* 375 (2004), pp. 213-218.
- [9] Z. Wu, H. Bei, F. Otto, G.M. Pharr, and E.P. George, *Recovery, recrystallization, grain growth and phase stability of a family of FCC-structured multi-component equiatomic solid solution alloys*, *Intermetallics* 46 (2014), pp. 131-140.
- [10] Z. Wu, H. Bei, G.M. Pharr, and E.P. George, *Temperature dependence of the mechanical properties of equiatomic solid solution alloys with face-centered cubic crystal structures*, *Acta Materialia* 81 (2014), pp. 428-441.

- [11] A. Gali, and E.P. George, *Tensile properties of high- and medium-entropy alloys*, Intermetallics 39 (2013), pp. 74-78.
- [12] F. Otto, A. Dlouhý, C. Somsen, H. Bei, G. Eggeler, and E.P. George, *The influences of temperature and microstructure on the tensile properties of a CoCrFeMnNi high-entropy alloy*, Acta Materialia 61 (2013), pp. 5743-5755.
- [13] B. Gludovatz, A. Hohenwarter, D. Catoor, E.H. Chang, E.P. George, and R.O. Ritchie, *A fracture-resistant high-entropy alloy for cryogenic applications*, Science 345 (2014), pp. 1153-1158.
- [14] M.Z. Butt, and P. Feltham, *Solid-solution hardening*, Journal of Materials Science 28 (1993), pp. 2557-2576.
- [15] F.R.N. Nabarro, *The Mechanical Properties of Metallic Solid Solutions*, Proceedings of the Physical Society of London 58 (1946), pp. 669-676.
- [16] R. Labusch, *A Statistical Theory of Solid Solution Hardening*, physica status solidi (b) 41 (1970), pp. 659-669.
- [17] N.L. Okamoto, K. Yuge, K. Tanaka, H. Inui, and E.P. George, *Atomic displacement in the CrMnFeCoNi high-entropy alloy – A scaling factor to predict solid solution strengthening*, AIP Advances 6 (2016).
- [18] L. Li, Q. Fang, J. Li, B. Liu, Y. Liu, and P.K. Liaw, *Lattice-distortion dependent yield strength in high entropy alloys*, Materials Science and Engineering: A 784 (2020).
- [19] O.N. Senkov, J.M. Scott, S.V. Senkova, D.B. Miracle, and C.F. Woodward, *Microstructure and room temperature properties of a high-entropy TaNbHfZrTi alloy*, Journal of Alloys and Compounds 509 (2011), pp. 6043-6048.
- [20] M. Mizuno, K. Sugita, and H. Araki, *Defect energetics for diffusion in CrMnFeCoNi high-entropy alloy from first-principles calculations*, Computational Materials Science 170 (2019).
- [21] L.R. Owen, and N.G. Jones, *Quantifying local lattice distortions in alloys*, Scripta Materialia 187 (2020), pp. 428-433.
- [22] J.-W. Yeh, S.-Y. Chang, Y.-D. Hong, S.-K. Chen, and S.-J. Lin, *Anomalous decrease in X-ray diffraction intensities of Cu–Ni–Al–Co–Cr–Fe–Si alloy systems with multi-principal elements*, Materials Chemistry and Physics 103 (2007), pp. 41-46.
- [23] Y. Zou, S. Maiti, W. Steurer, and R. Spolenak, *Size-dependent plasticity in an Nb<sub>25</sub>Mo<sub>25</sub>Ta<sub>25</sub>W<sub>25</sub> refractory high-entropy alloy*, Acta Materialia 65 (2014), pp. 85-97.
- [24] L.R. Owen, E.J. Pickering, H.Y. Playford, H.J. Stone, M.G. Tucker, and N.G. Jones, *An assessment of the lattice strain in the CrMnFeCoNi high-entropy alloy*, Acta Materialia 122 (2017), pp. 11-18.
- [25] Y. Zhang, Y.J. Zhou, J.P. Lin, G.L. Chen, and P.K. Liaw, *Solid-Solution Phase Formation Rules for Multi-component Alloys*, Advanced Engineering Materials 10 (2008), pp. 534-538.
- [26] C. Li, Y. Xue, M. Hua, T. Cao, L. Ma, and L. Wang, *Microstructure and mechanical properties of*

- Al<sub>x</sub>Si<sub>0.2</sub>CrFeCoNiCu<sub>1-x</sub> high-entropy alloys*, Materials & Design 90 (2016), pp. 601-609.
- [27] S.S. Sohn, A. Kwiatkowski da Silva, Y. Ikeda, F. Kormann, W. Lu, W.S. Choi, B. Gault, D. Ponge, J. Neugebauer, and D. Raabe, *Ultrastrong Medium-Entropy Single-Phase Alloys Designed via Severe Lattice Distortion*, Adv Mater 31 (2019), p. e1807142.
- [28] S. Mu, S. Wimmer, S. Mankovsky, H. Ebert, and G.M. Stocks, *Influence of local lattice distortions on electrical transport of refractory high entropy alloys*, Scripta Materialia 170 (2019), pp. 189-194.
- [29] A.J.C.W. W. Parrish, J.I. Langford, *International Tables for Crystallography Volume C Third Edition*, (2004), pp. 498-504.
- [30] *Standard Reference Material 660c*.
- [31] H.S. Avner, *Introduction to physical metallurgy*, McGRAW-HILL KOGAKUSHA, LTD., Tokyo, 1974.
- [32] V.M. Goldschmidt, *On distances between atoms in metals.*, Zeitschrift Fur Physikalische Chemie-Stoichiometrie Und Verwandtschaftslehre 133 (1928), pp. 397-419.
- [33] G. Laplanche, P. Gadaud, C. Bärsch, K. Demtröder, C. Reinhart, J. Schreuer, and E.P. George, *Elastic moduli and thermal expansion coefficients of medium-entropy subsystems of the CrMnFeCoNi high-entropy alloy*, Journal of Alloys and Compounds 746 (2018), pp. 244-255.
- [34] S. Fang, X. Xiao, L. Xia, W. Li, and Y. Dong, *Relationship between the widths of supercooled liquid regions and bond parameters of Mg-based bulk metallic glasses*, Journal of Non-Crystalline Solids 321 (2003), pp. 120-125.

## Tables

Table 1 Composition of the experimental samples

(a) Objective value of sample composition (at.%)

	Base	Cr+	Cr-	Mn+	Mn-	Fe+	Fe-	Co+	Co-	Ni+	Ni-
Cr	20	25	15	18.75	21.25	18.75	21.25	18.75	21.25	18.75	21.25
Mn	20	18.75	21.25	25	15	18.75	21.25	18.75	21.25	18.75	21.25
Fe	20	18.75	21.25	18.75	21.25	25	15	18.75	21.25	18.75	21.25
Co	20	18.75	21.25	18.75	21.25	18.75	21.25	25	15	18.75	21.25
Ni	20	18.75	21.25	18.75	21.25	18.75	21.25	18.75	21.25	25	15

(b) Average composition of the prepared samples (at.%)

	Base	Cr+	Cr-	Mn+	Mn-	Fe+	Fe-	Co+	Co-	Ni+	Ni-
Cr	20.2	25.8	15.0	18.9	21.3	18.4	21.3	18.8	21.5	18.9	21.3
Mn	20.1	18.7	21.0	24.8	15.3	18.8	21.5	18.5	21.0	18.6	21.1
Fe	20.4	19.1	21.7	19.5	21.4	25.5	15.4	19.1	21.7	19.4	21.8
Co	20.3	19.2	22.0	19.2	21.7	19.6	21.7	25.9	15.7	19.5	21.8
Ni	19.0	17.3	20.3	17.6	20.3	17.7	20.1	17.7	20.1	23.6	14.1

Table 2 Effective lattice parameter ( $a_{\text{eff}}$ ) and atomic radius ( $r_{\text{eff}}$ ) in CrMnFeCoNi high entropy alloy at 22.50 °C

	(pm)				
	Cr	Mn	Fe	Co	Ni
$a_{\text{eff}}$	357.82	370.51	357.56	352.40	361.23
$r_{\text{eff}}$	126.5(4)	131.0(4)	126.4(4)	124.6(4)	127.7(4)

Table 3 Comparison between the experimental and analytical values of the atomic radii

Atomic radius (pm) Small ↓ Large	Experimental value		Goldschmidt[17]		Ab initio calculation[17]	
	Co	124.6(4)	Mn	124.0	Co	121.9
	Fe	126.4(4)	Fe	124.1	Fe	121.9
	Cr	126.5(4)	Ni	124.6	Mn	123.5
	Ni	127.7(4)	Cr	124.9	Ni	123.9
	Mn	131.0(4)	Co	125.3	Cr	126.9

## Figures

Figure 1 Temperature control stage of XRD

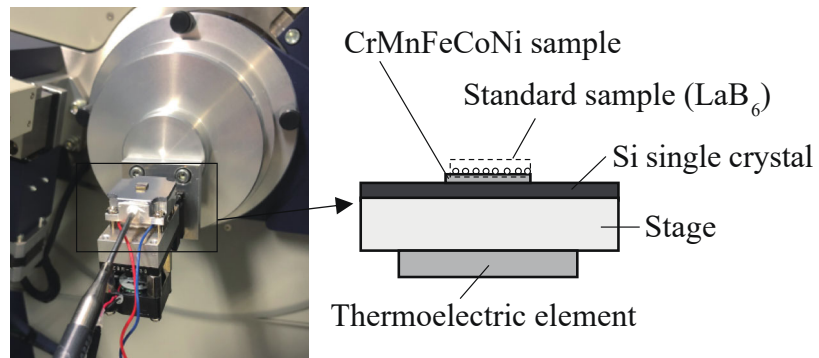


Figure 2 XRD patterns. The lattice parameters were determined from the five peaks hatched in gray. Peaks of standard samples are shown with Std. subscript.

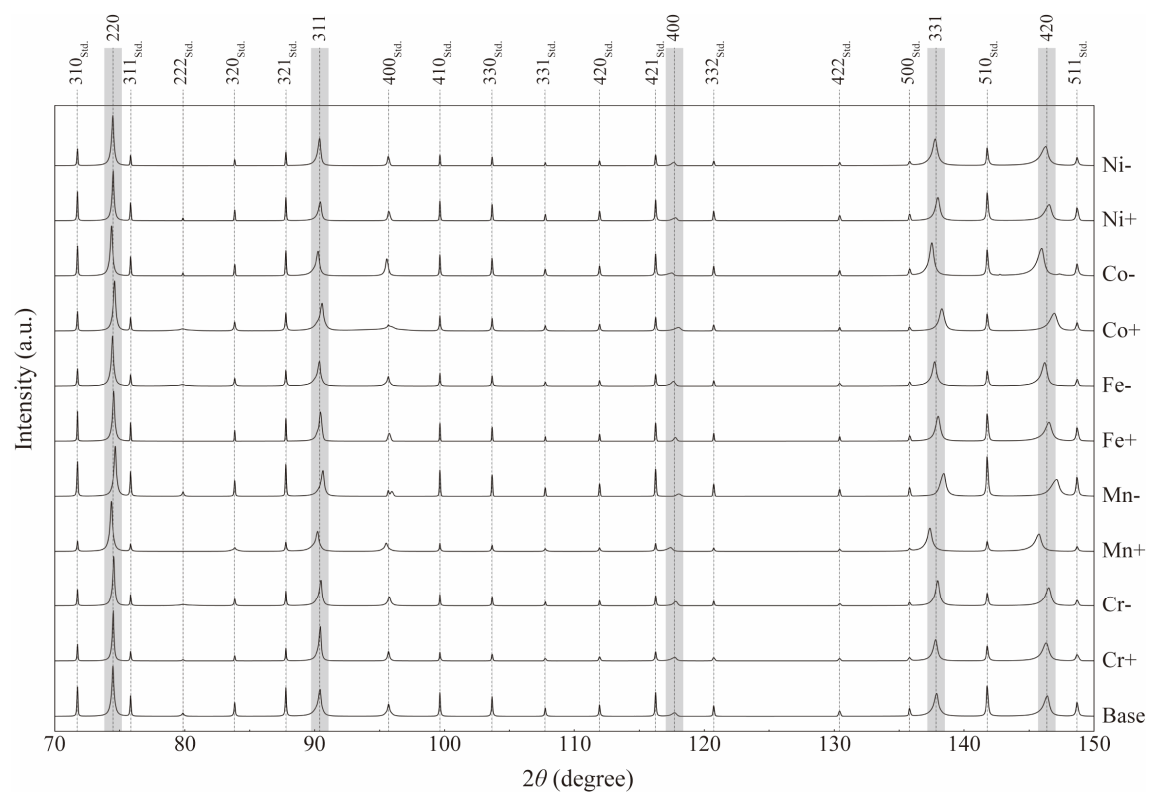
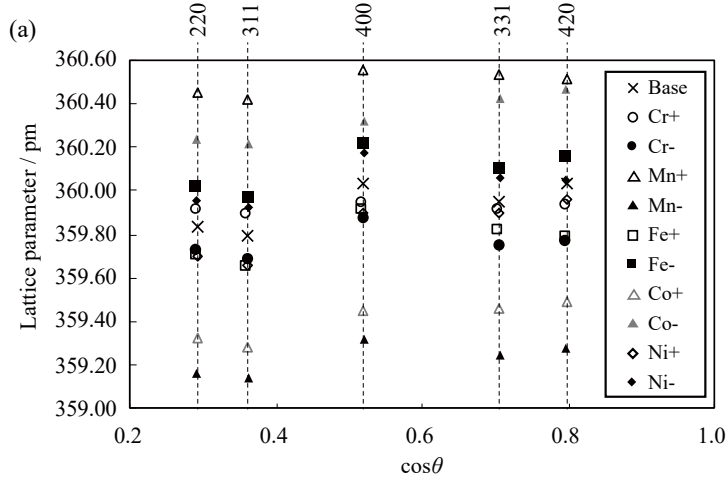




Figure 3 Lattice parameter measurement. (a) Variation in the lattice parameter for each constituent.

(b) Determined lattice parameter (pm) for all the constituents. The standard deviation is enclosed within parentheses.



(b)

Base	359.93(10)	
	+	□
Cr	359.92(2)	359.76(6)
Mn	360.49(5)	359.23(7)
Fe	359.77(9)	360.09(9)
Co	359.40(9)	360.34(10)
Ni	359.83(12)	360.04(9)

Figure 4 Relationship between the experimental and predicted lattice parameters obtained via the multiple regression analysis

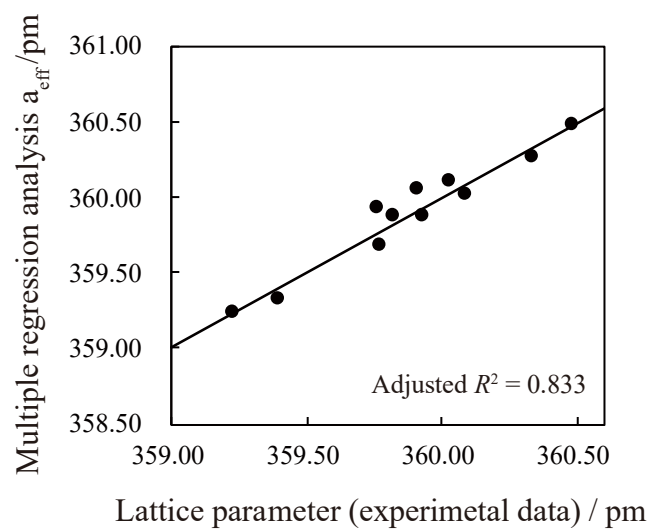


Figure 5 Relationship between the yield stress and average atomic displacement ( $\delta r$ ) for the CrMnFeCoNi system

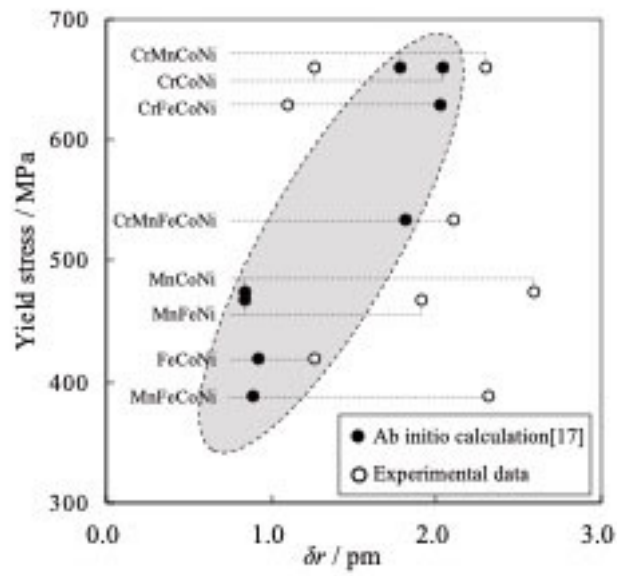


Figure 1 Temperature control stage of XRD

Figure 2 XRD patterns. The lattice parameters were determined from the five peaks hatched in gray. Peaks of standard samples are shown with Std. subscript.

Figure 3 Lattice parameter measurement. (a) Variation in the lattice parameter for each constituent.

(b) Determined lattice parameter (pm) for all the constituents. The standard deviation is enclosed within parentheses.

Figure 4 Relationship between the experimental and predicted lattice parameters obtained via the multiple regression analysis

Figure 5 Relationship between the yield stress and average atomic displacement ( $\delta r$ ) for the CrMnFeCoNi system